INTERNATIONAL JOURNAL FOR NUMERICAL METHODS IN ENGINEERING Vol. 66, Iss 9, Date: 28 May 2006, Pages: 1466-1482

Int. J. Numer. Meth. Engng 2000; **00**:1 *Prepared using* nmeauth.cls *[Version: 2002/09/18 v2.02]*

Non-Conservative and Conservative Formulations of Characteristics-Based Numerical Reconstructions for Incompressible Flows

E. Shapiro, D. Drikakis

Fluid Mechanics and Computational Science Group

Aerospace Sciences Department, Cranfield University,

Cranfield, Bedfordshire, MK43 0AL, United Kingdom

SUMMARY

An investigation of characteristics-based (CB) schemes for solving the incompressible Navier-Stokes equations in conjunction with the artificial-compressibility approach, is presented. Both non-conservative and conservative characteristics-based numerical reconstructions are derived and their accuracy and convergence properties are assessed analytically and numerically. We demonstrate by means of eigenvalue analysis that there are differences in the spectral characteristics of these formulations that result in different convergence properties. Numerical tests for two- and three-dimensional flows reveal that the two formulations provide similar accuracy but the non-conservative formulation converges faster.

KEY WORDS: Incompressible flows; characteristics-based scheme; Riemann solvers; high-resolution methods; eigenvalue analysis

Received

Revised

1. INTRODUCTION

One of the difficulties when dealing with the computation of incompressible flows is the decoupling of the continuity and momentum equations due to the absence of the pressure (or density) term from the former. Two different approaches that have received attention for solving the incompressible equations are the artificial-compressibility approach [1] and projection methods [2, 4, 5], approximate and exact. The projection formulation also shares similarities with the pressure-Poisson approach [6]. A review of the artificial-compressibility and projection methods can be found in [3].

The growing interest in the artificial compressibility approach is partly due to the direct coupling of continuity and momentum equations, which allows the use of explicit schemes and facilitates the development of memory-efficient easily parallelisable solvers. Recent examples of efficient numerical schemes utilising the artificial compressibility approach can be found in [7, 8], where a characteristics-based split finite element scheme has been modified to create an efficient fully explicit solver; in [9, 10], where an artificial compressibility scheme utilising vertex-centred and dual-cell, edge-based spatial discretisation, has been developed; as well as in [11, 12] where a characteristics-based (CB) scheme [13] has been combined with multigrid strategies to provide efficient solutions for two- and the three-dimensional flows.

The discretisation schemes and solvers developed for artificial compressibility have many similarities with the methods developed for compressible flows. In particular, artificial compressibility coupling facilitates the use of high-resolution Godunov-type schemes for incompressible flows [3]. An example of Godunov-type method used both for incompressible and compressible flows, is the CB scheme of [14], which was extended to incompressible flows by Drikakis et al. [13, 3]. The CB scheme has been proven to provide accurate solutions in

a broad range of Reynolds numbers for applications including Newtonian [12, 11] and non-Newtonian flows [15, 16]; flows in porous media [17]; unstructured grid implementations [18]; high-Reynolds number turbomachinery flows [19]; large eddy simulation [20] and variable-density multi-species flows [21, 22].

In the present paper we show that two different formulations of the CB scheme can be derived for incompressible flows. One formulation uses the divergence-free condition in the numerical reconstruction of the primitive variables, whereas the other does not. These formulations result in different high-resolution, Godunov-type schemes. Improving the efficiency of a numerical solution is of crucial importance both in two- and three-dimensional simulations, especially when multi-parametric investigations (geometry or physics related) are required. Here, we present a unified formulation for conservative and non-conservative CB schemes, carry out eigenvalue analysis to study the effects of these schemes on convergence and further perform two- and three-dimensional computations for test problems to examine the the accuracy and efficiency of the schemes.

The paper is organised as follows. Section 2 presents the derivation of conservative and non-conservative CB schemes for incompressible flows as well as the computational strategy employed in this paper for solving the incompressible Navier-Stokes equations. Section 3 presents the eigenvalue analysis for the two CB schemes. Numerical tests demonstrating accuracy and efficiency issues are presented in Section 4. Finally, Section 5 summarises the conclusions of the present work.

2. CHARACTERISTICS-BASED SCHEMES

2.1. Problem Formulation

We consider the artificial compressibility formulation for the incompressible Navier-Stokes equations [1] and write the equations in conservative form, for the variables vector $\mathbf{U} = \left(\frac{p}{\beta}, u, v, w\right)^T$, where β is the artificial compressibility parameter, then in Cartesian coordinates (x, y, z),

$$\frac{\partial \mathbf{U}}{\partial \tau} = \frac{\partial \mathbf{E_V^c}}{\partial x} + \frac{\partial \mathbf{F_V^c}}{\partial y} + \frac{\partial \mathbf{G_V^c}}{\partial z} - \frac{\partial \mathbf{E_I^c}}{\partial x} - \frac{\partial \mathbf{F_I^c}}{\partial y} - \frac{\partial \mathbf{G_I^c}}{\partial z}, \tag{1}$$

where the inviscid $(\mathbf{E_I^c}, \mathbf{F_I^c}, \mathbf{G_I^c})$ and viscous $(\mathbf{E_V^c}, \mathbf{F_V^c}, \mathbf{G_V^c})$ flux vectors are given by

$$\begin{cases} \mathbf{E_I^c} &= \left(u, u^2 + p, uv, uw\right)^T \\ \mathbf{F_I^c} &= \left(v, uv, v^2 + p, vw\right)^T \\ \mathbf{G_I^c} &= \left(w, uw, vw, w^2 + p\right)^T \\ \mathbf{E_V^c} &= \left(0, \tau_{xx}, \tau_{xy}, \tau_{xz}\right)^T \\ \mathbf{F_V^c} &= \left(0, \tau_{yx}, \tau_{yy}, \tau_{yz}\right)^T \\ \mathbf{G_V^c} &= \left(0, \tau_{zx}, \tau_{zy}, \tau_{zz}\right)^T \end{cases} . \tag{2}$$

In the above equations τ_{ij} stands for the viscous stresses. We consider an arbitrary curvilinear system $(\xi(x, y, z), \eta(x, y, z), \zeta(x, y, z))$ where the Jacobian of the transformation is given by $J = \left|\frac{\partial(x,y,z)}{\partial(\xi,\eta,\zeta)}\right|$. The system of (1) can be written in curvilinear coordinates as

$$\frac{\partial J\mathbf{U}}{\partial \tau} = \frac{\partial \mathbf{E_V}}{\partial \xi} + \frac{\partial \mathbf{F_V}}{\partial \eta} + \frac{\partial \mathbf{G_V}}{\partial \zeta} - \frac{\partial \mathbf{E_I}}{\partial \xi} - \frac{\partial \mathbf{F_I}}{\partial \eta} - \frac{\partial \mathbf{G_I}}{\partial \zeta} . \tag{3}$$

The inviscid, $(\mathbf{E_I}, \mathbf{F_I}, \mathbf{G_I})$, and viscous, $(\mathbf{E_V}, \mathbf{F_V}, \mathbf{G_V})$, fluxes in the curvilinear system are given by

$$\left\{\begin{array}{l} \mathbf{E_I} = J\left(\mathbf{E_I^c}\frac{\partial\xi}{\partial x} + \mathbf{F_I^c}\frac{\partial\xi}{\partial y} + \mathbf{G_I^c}\frac{\partial\xi}{\partial z}\right) \\ \mathbf{F_I} = J\left(\mathbf{E_I^c}\frac{\partial\eta}{\partial x} + \mathbf{F_I^c}\frac{\partial\eta}{\partial y} + \mathbf{G_I^c}\frac{\partial\eta}{\partial z}\right) \\ \mathbf{G_I} = J\left(\mathbf{E_I^c}\frac{\partial\zeta}{\partial x} + \mathbf{F_I^c}\frac{\partial\zeta}{\partial y} + \mathbf{G_I^c}\frac{\partial\zeta}{\partial z}\right) \\ \mathbf{E_V} = J\left(\mathbf{E_V^c}\frac{\partial\xi}{\partial x} + \mathbf{F_V^c}\frac{\partial\xi}{\partial y} + \mathbf{G_V^c}\frac{\partial\xi}{\partial z}\right) \\ \mathbf{F_V} = J\left(\mathbf{E_V^c}\frac{\partial\eta}{\partial x} + \mathbf{F_V^c}\frac{\partial\eta}{\partial y} + \mathbf{G_V^c}\frac{\partial\eta}{\partial z}\right) \\ \mathbf{G_V} = J\left(\mathbf{E_V^c}\frac{\partial\zeta}{\partial x} + \mathbf{F_V^c}\frac{\partial\zeta}{\partial y} + \mathbf{G_V^c}\frac{\partial\zeta}{\partial z}\right) \end{array}\right. \tag{4}$$

In the numerical reconstruction of the advective fluxes one can employ dimensional splitting. In this work, dimensional splitting is used only for analytically deriving characteristics-based formulae for the intercell variables, which in turn are used to calculate the advective fluxes. The time integration is obtained for the complete system of equations after adding all the discretised fluxes (inviscid and viscous), using an explicit time integration scheme (see discussion below). In order to derive CB reconstructions we consider the one-dimensional counterpart of (3), e.g., with respect to the ξ-direction (non-moving grids are considered throughout)

$$\frac{\partial\mathbf{U}}{\partial\tau} + \frac{\partial\xi}{\partial x}\frac{\partial\mathbf{E_I^c}}{\partial\xi} + \frac{\partial\xi}{\partial y}\frac{\partial\mathbf{F_I^c}}{\partial\xi} + \frac{\partial\xi}{\partial z}\frac{\partial\mathbf{G_I^c}}{\partial\xi} = 0\,, \tag{5}$$

We divide the above equation by $\sqrt{\left(\frac{\partial\xi}{\partial x}\right)^2 + \left(\frac{\partial\xi}{\partial y}\right)^2 + \left(\frac{\partial\xi}{\partial z}\right)^2}$ and introduce the notation $L = \sqrt{\left(\frac{\partial\xi}{\partial x}\right)^2 + \left(\frac{\partial\xi}{\partial y}\right)^2 + \left(\frac{\partial\xi}{\partial z}\right)^2}$ and $\widetilde{k} = \frac{1}{L}\frac{\partial\xi}{\partial k}$, where $k = x, y, z$, thus obtaining

$$\left\{\begin{array}{c} \frac{1}{\beta L}\frac{\partial p}{\partial\tau} + \widetilde{x}\frac{\partial u}{\partial\xi} + \widetilde{y}\frac{\partial v}{\partial\xi} + \widetilde{z}\frac{\partial w}{\partial\xi} = 0 \\ \frac{1}{L}\frac{\partial u}{\partial\tau} + (u\widetilde{x} + v\widetilde{y} + w\widetilde{z})\frac{\partial u}{\partial\xi} + \left(\widetilde{x}\frac{\partial u}{\partial\xi} + \widetilde{y}\frac{\partial v}{\partial\xi} + \widetilde{z}\frac{\partial w}{\partial\xi}\right)u + \frac{\partial p}{\partial\xi}\widetilde{x} = 0 \\ \frac{1}{L}\frac{\partial v}{\partial\tau} + (u\widetilde{x} + v\widetilde{y} + w\widetilde{z})\frac{\partial v}{\partial\xi} + \left(\widetilde{x}\frac{\partial u}{\partial\xi} + \widetilde{y}\frac{\partial v}{\partial\xi} + \widetilde{z}\frac{\partial w}{\partial\xi}\right)v + \frac{\partial p}{\partial\xi}\widetilde{y} = 0 \\ \frac{1}{L}\frac{\partial w}{\partial\tau} + (u\widetilde{x} + v\widetilde{y} + w\widetilde{z})\frac{\partial w}{\partial\xi} + \left(\widetilde{x}\frac{\partial u}{\partial\xi} + \widetilde{y}\frac{\partial v}{\partial\xi} + \widetilde{z}\frac{\partial w}{\partial\xi}\right)w + \frac{\partial p}{\partial\xi}\widetilde{z} = 0 \end{array}\right. . \tag{6}$$

Another formulation can be obtained if the continuity equation is used to simplify the momentum equations prior to the addition of the pseudo-time derivative in the former,

$$\begin{cases} \widetilde{x}\frac{\partial u}{\partial \xi} + \widetilde{y}\frac{\partial v}{\partial \xi} + \widetilde{z}\frac{\partial w}{\partial \xi} = 0 \\ \frac{1}{L}\frac{\partial u}{\partial \tau} + (u\widetilde{x} + v\widetilde{y} + w\widetilde{z})\frac{\partial u}{\partial \xi} + \frac{\partial p}{\partial \xi}\widetilde{x} = 0 \\ \frac{1}{L}\frac{\partial v}{\partial \tau} + (u\widetilde{x} + v\widetilde{y} + w\widetilde{z})\frac{\partial v}{\partial \xi} + \frac{\partial p}{\partial \xi}\widetilde{y} = 0 \\ \frac{1}{L}\frac{\partial w}{\partial \tau} + (u\widetilde{x} + v\widetilde{y} + w\widetilde{z})\frac{\partial w}{\partial \xi} + \frac{\partial p}{\partial \xi}\widetilde{z} = 0 \end{cases} . \tag{7}$$

Adding the pseudo-time pressure derivative to the continuity equation yields

$$\begin{cases} \frac{1}{\beta L}\frac{\partial p}{\partial \tau} + \widetilde{x}\frac{\partial u}{\partial \xi} + \widetilde{y}\frac{\partial v}{\partial \xi} + \widetilde{z}\frac{\partial w}{\partial \xi} = 0 \\ \frac{1}{L}\frac{\partial u}{\partial \tau} + (u\widetilde{x} + v\widetilde{y} + w\widetilde{z})\frac{\partial u}{\partial \xi} + \frac{\partial p}{\partial \xi}\widetilde{x} = 0 \\ \frac{1}{L}\frac{\partial v}{\partial \tau} + (u\widetilde{x} + v\widetilde{y} + w\widetilde{z})\frac{\partial v}{\partial \xi} + \frac{\partial p}{\partial \xi}\widetilde{y} = 0 \\ \frac{1}{L}\frac{\partial w}{\partial \tau} + (u\widetilde{x} + v\widetilde{y} + w\widetilde{z})\frac{\partial w}{\partial \xi} + \frac{\partial p}{\partial \xi}\widetilde{z} = 0 \end{cases} . \tag{8}$$

Equations (6) and (8) consist two different formulations of the artificial-compressibility equations, with the former encompassing velocity divergence terms in the momentum equations. Henceforth, we will refer to the systems (6) and (8) as *conservative* and *non-conservative* formulations, respectively.

Using the above two formulations as a starting point, in the next section we derive two different CB schemes. We will show that although both formulations yield similar results for the solution of the incompressible Navier-Stokes equations, the eigenstructure of the systems (6) and (8) is different thus leading to different convergence properties. The systems (6) and (8) are used solely for the CB reconstruction of the advective flux in $\xi-$direction and a similar procedure can be used for the fluxes in the other two directions. Once the fluxes are discretised, the actual system equations which is numerically integrated is the conservative equations (3).

The present paper focuses on the implementation of conservative and non-conservative CB formulations in block-structured grids but CB schemes can also be implemented in conjunction with unstructured mesh as discussed in [18, 3]; in [18] the conservative CB scheme has been implemented in fully unstructured meshes.

2.2. Variables Reconstruction

The advective and viscous fluxes are discretised on the cell centres using the intercell values, e.g., the inviscid flux derivative in the $\xi-$direction is given by

$$\frac{\partial \mathbf{E_I}}{\partial \xi} = \frac{(\mathbf{E_I})_{i+\frac{1}{2},j,k} - (\mathbf{E_I})_{i-\frac{1}{2},j,k}}{\Delta \xi} \, . \tag{9}$$

Both the conservative (6) and non-conservative (8) formulations can be written in a unified form,

$$\begin{cases} \frac{1}{\beta L}\frac{\partial p}{\partial \tau} + \widetilde{x}\frac{\partial u}{\partial \xi} + \widetilde{y}\frac{\partial v}{\partial \xi} + \widetilde{z}\frac{\partial w}{\partial \xi} = 0 \\ \frac{1}{L}\frac{\partial u}{\partial \tau} + (u\widetilde{x} + v\widetilde{y} + w\widetilde{z})\frac{\partial u}{\partial \xi} + \delta\left(\widetilde{x}\frac{\partial u}{\partial \xi} + \widetilde{y}\frac{\partial v}{\partial \xi} + \widetilde{z}\frac{\partial w}{\partial \xi}\right)u + \frac{\partial p}{\partial \xi}\widetilde{x} = 0 \\ \frac{1}{L}\frac{\partial v}{\partial \tau} + (u\widetilde{x} + v\widetilde{y} + w\widetilde{z})\frac{\partial v}{\partial \xi} + \delta\left(\widetilde{x}\frac{\partial u}{\partial \xi} + \widetilde{y}\frac{\partial v}{\partial \xi} + \widetilde{z}\frac{\partial w}{\partial \xi}\right)v + \frac{\partial p}{\partial \xi}\widetilde{y} = 0 \\ \frac{1}{L}\frac{\partial w}{\partial \tau} + (u\widetilde{x} + v\widetilde{y} + w\widetilde{z})\frac{\partial w}{\partial \xi} + \delta\left(\widetilde{x}\frac{\partial u}{\partial \xi} + \widetilde{y}\frac{\partial v}{\partial \xi} + \widetilde{z}\frac{\partial w}{\partial \xi}\right)w + \frac{\partial p}{\partial \xi}\widetilde{z} = 0 \end{cases} . \tag{10}$$

where the coefficient δ takes the values $\delta = 1$ and $\delta = 0$ for the conservative and non-conservative formulations, respectively. The system (10) can also be written in matrix-form

$$\frac{1}{L}\frac{\partial \mathbf{U}}{\partial \tau} + \mathbf{A}\frac{\partial \mathbf{U}}{\partial \xi} = 0 \, . \tag{11}$$

The matrix $\mathbf{A}$ is given by

$$\mathbf{A} = \begin{pmatrix} 0 & \widetilde{x} & \widetilde{y} & \widetilde{z} \\ \widetilde{x} & \lambda_0 + \widetilde{x}u\delta & u\widetilde{y}\delta & u\widetilde{z}\delta \\ \widetilde{y} & \widetilde{x}v\delta & \lambda_0 + \widetilde{y}v\delta & v\widetilde{z}\delta \\ \widetilde{z} & \widetilde{x}w\delta & w\widetilde{y}\delta & \lambda_0 + \widetilde{z}w\delta \end{pmatrix}. \tag{12}$$

where $\lambda_0 = u\widetilde{x} + v\widetilde{y} + w\widetilde{z}$ denotes velocity normal to the cell face. The eigenvalues of this matrix are given by λ_0 and $\lambda_\pm$ where

$$\lambda_\pm = \lambda_{1,2} = \lambda_0 \tfrac{(1+\delta)}{2} \pm s \ , \tag{13}$$

and the artificial speed of sound s is given by

$$s = \frac{\sqrt{\lambda_0^2 (1+\delta)^2 + 4\beta}}{2}. \tag{14}$$

Following the same derivation procedure as for the original CB scheme ([13, 3]), we obtain the following formulae for the reconstructed variables at the cell face $(\widetilde{p}, \widetilde{u}, \widetilde{v}, \widetilde{w})$:

$$\begin{cases} \widetilde{p} = \frac{1}{\lambda_+ - \lambda_-} \left(p_- \lambda_+ - p_+ \lambda_- + \lambda_+ \lambda_- \left(R_+ - R_- \right) \right) \\ \widetilde{u} = u_0 + \frac{\widetilde{x}}{(\lambda_+ - \lambda_-)} \left(p_+ - p_- - \lambda_+ R_+ + \lambda_- R_- \right) \\ \widetilde{u} = u_0 + \frac{\widetilde{x}}{(\lambda_+ - \lambda_-)} \left(p_+ - p_- - \lambda_+ R_+ + \lambda_- R_- \right) \\ \widetilde{w} = w_0 + \frac{\widetilde{z}}{(\lambda_+ - \lambda_-)} \left(p_+ - p_- - \lambda_+ R_+ + \lambda_- R_- \right) \end{cases}, \tag{15}$$

where R_+ and R_- are the auxiliary functions

$$\begin{cases} R_+ = \widetilde{x} \left(u_0 - u_+ \right) + \widetilde{y} \left(v_0 - v_+ \right) + \widetilde{z} \left(w_0 - w_+ \right) \\ R_- = \widetilde{x} \left(u_0 - u_- \right) + \widetilde{y} \left(v_0 - v_- \right) + \widetilde{z} \left(w_0 - w_- \right) \end{cases}. \tag{16}$$

The variables with the subscript $\pm$ are defined from the left and right states depending on the sign of the corresponding eigenvalue, i.e.,

$$\begin{cases} \mathbf{U}_0 = \frac{\mathbf{U}_L+\mathbf{U}_R}{2} - \text{sign}\left(\lambda_0\right)\frac{\mathbf{U}_R-\mathbf{U}_L}{2} \\ \mathbf{U}_- = \mathbf{U}_R \\ \mathbf{U}_+ = \mathbf{U}_L \end{cases} . \tag{17}$$

In the present work, the left and right states $\mathbf{U}_{L,R}$ are calculated by third order interpolation (see [3] for more details). The CB scheme given by (15) is applicable to both steady and unsteady flows. In the case of unsteady computations the dual time-stepping approach can be used in conjunction with the artificial-compressibility. According to the dual-time stepping approach, pseudo-time derivatives are added to both continuity and momentum equations [3]. The equations are solved at each real time step by driving the discretised pseudo-time derivatives to the machine zero. The real time derivatives are treated as source terms and can be discretised by first or higher-order differences.

The reconstructed variables at the cell faces are used to compute the advective fluxes in (9). The viscous fluxes are approximated by central differences. The numerical time integration was obtained by a fourth order accurate explicit Runge-Kutta scheme [23]. A full multigrid - full approximation storage algorithm (FMG-FAS) is also used to accelerate numerical convergence [12, 3]. The multigrid strategy employed here comprises of three V-cycles, ten pre-smoothing and post-relaxation iterations on the fine grid, five post-relaxation iterations on the intermediate grid and five hundred iterations on the coarse grid. Details of the multigrid algorithm used in this study can be found in [12].

3. EIGENVALUE ANALYSIS

In this section we compare the spectral radius and characteristic condition numbers of the two variants of the chracteristics-based scheme. The spectral radius provides information about the maximum stable pseudo-time step, while the characteristic condition number is a measure of numerical stiffness. We consider first the conservative reconstruction for which $\delta = 0$; the eigenvalues (13) are given by

$$\begin{cases} \lambda_0 = u\widetilde{x} + v\widetilde{y} + w\widetilde{z} \\ \lambda_+ = \frac{\lambda_0 + \sqrt{\lambda_0^2 + 4\beta}}{2} \\ \lambda_- = \frac{\lambda_0 - \sqrt{\lambda_0^2 + 4\beta}}{2} \end{cases} . \tag{18}$$

When the velocity normal to the cell face is positive $\lambda_0 > 0$ ($|\lambda_0| = \lambda_0$), we obtain

$$\lambda_+ = \frac{|\lambda_0| + \sqrt{|\lambda_0|^2 + 4\beta}}{2} > |\lambda_0| \tag{19}$$

and

$$\lambda_- = \frac{|\lambda_0| - \sqrt{|\lambda_0|^2 + 4\beta}}{2} < 0. \tag{20}$$

Comparing λ_+ and λ_- yields

$$|\lambda_-| = \frac{\sqrt{|\lambda_0|^2 + 4\beta} - |\lambda_0|}{2} < \frac{\sqrt{|\lambda_0|^2 + 4\beta} + |\lambda_0|}{2} = |\lambda_+| . \tag{21}$$

Also, when $\beta > 2\lambda_0^2$

$$|\lambda_-| = \sqrt{\frac{|\lambda_0|^2}{4} + \beta} - \frac{|\lambda_0|}{2} > |\lambda_0| . \tag{22}$$

Therefore, we can write

$$\begin{cases} |\lambda_0| < |\lambda_-| < |\lambda_+| & \text{when} \quad \beta > 2\lambda_0^2 \\ |\lambda_-| < |\lambda_0| < |\lambda_+| & \text{when} \quad \beta \leq 2\lambda_0^2 \end{cases} \tag{23}$$

When the velocity normal to the cell face is negative $\lambda_0 < 0$ ($|\lambda_0| = -\lambda_0$), we obtain

$$\lambda_+ = \frac{\lambda_0 + \sqrt{\lambda_0^2 + 4\beta}}{2} = \frac{-|\lambda_0| + \sqrt{|\lambda_0|^2 + 4\beta}}{2} > 0, \tag{24}$$

$$\lambda_- = \frac{\lambda_0 - \sqrt{\lambda_0^2 + 4\beta}}{2} = \frac{-|\lambda_0| - \sqrt{|\lambda_0|^2 + 4\beta}}{2} < 0. \tag{25}$$

Comparing the absolute values of $\lambda_\pm$ yields

$$|\lambda_-| = \frac{\sqrt{|\lambda_0|^2 + 4\beta} + |\lambda_0|}{2} > \frac{\sqrt{|\lambda_0|^2 + 4\beta} - |\lambda_0|}{2} = |\lambda_+| \,. \tag{26}$$

Similarly, when $\beta > 2\lambda_0^2$

$$|\lambda_+| = \sqrt{\frac{|\lambda_0|^2}{4} + \beta} - \frac{|\lambda_0|}{2} > |\lambda_0| \ . \tag{27}$$

Therefore, we can write

$$\begin{cases} |\lambda_0| < |\lambda_+| < |\lambda_-| & \text{when} \quad \beta > 2\lambda_0^2 \\ |\lambda_+| < |\lambda_0| < |\lambda_-| & \text{when} \quad \beta \leq 2\lambda_0^2 \end{cases} \tag{28}$$

From equations (23) and (28) we obtain the following formula for the spectral radius of the non-conservative formulation

$$\rho_{NC} = \max |\lambda_i| = \frac{|\lambda_0| + \sqrt{\lambda_0^2 + 4\beta}}{2} \tag{29}$$

The characteristic condition number for this case is given by

$$K_{NC} = \begin{cases} \frac{\sqrt{\lambda_0^2+4\beta}+|\lambda_0|}{2|\lambda_0|} & \beta > 2\lambda_0^2 \\ \frac{\sqrt{\lambda_0^2+4\beta}+|\lambda_0|}{\sqrt{\lambda_0^2+4\beta}-|\lambda_0|} & \beta \leq 2\lambda_0^2 \end{cases} \tag{30}$$

Similar analysis for the conservative formulation yields the following formulae for the spectral radius and characteristic condition numbers

$$\rho_C = \max|\lambda_i| = |\lambda_0| + \sqrt{\lambda_0^2+\beta} \tag{31}$$

$$K_C = \begin{cases} \frac{\sqrt{\lambda_0^2+\beta}+|\lambda_0|}{|\lambda_0|} & \beta > 3\lambda_0^2 \\ \frac{\sqrt{\lambda_0^2+\beta}+|\lambda_0|}{\sqrt{\lambda_0^2+\beta}-|\lambda_0|} & \beta \leq 3\lambda_0^2 \end{cases} \tag{32}$$

We shall now show that the spectral radius of the conservative formulation is greater than that of the non-conservative formulation. We consider $\rho = \rho(|\lambda_0|)$ for both formulations and note that these functions have uniformly positive derivatives for any (positive) value of β. Moreover, from (29) and (31) it can be seen that $\rho_{NC}(|\lambda_0|) = \rho_C(|\lambda_0|/2)$, therefore $\rho_C(|\lambda_0|) > \rho_{NC}(|\lambda_0|)$ for any $|\lambda_0|$, i.e., the spectral radius of the system matrix is greater in the case of the conservative formulation.

One immediate consequence of the above is that when local time stepping is employed, the non-conservative formulation allows the use of larger time steps. For the same CFL number, the ratio of the maximum possible local time step for the conservative and non-conservative schemes is given by:

$$R_t(|\lambda_0|,\beta) = \frac{\Delta t_{NC}}{\Delta t_C} = \frac{\rho_C(|\lambda_0|,\beta)}{\rho_{NC}(|\lambda_0|,\beta)} = 2\frac{|\lambda_0| + \sqrt{\lambda_0^2+\beta}}{|\lambda_0| + \sqrt{\lambda_0^2+4\beta}} \tag{33}$$

By normalising λ_0 with $\sqrt{\beta}$ and introducing the similarity variable $r = |\lambda_0|/\sqrt{\beta}$, the ratio of time steps can be written as a function of r:

$$R_t\left(r\right) = 2\frac{r+\sqrt{r^2+1}}{r+\sqrt{r^2+4}} \tag{34}$$

For the flow regions where the velocity (normal to the cell face) tends to zero, R_t tends to 1 and R_t is a monotonously increasing function of r, i.e., $\frac{dR_t}{dr} > 0$ for any value of r, with an asymptote of 2 at infinity. Therefore, one should expect the differences in numerical convergence between the two schemes to be larger for smaller values of β as well as when the local flow speed is higher (Fig. 1a).

The characteristic condition number is considered to be a measure of numerical stiffness. In terms of the similarity variable r, we can express the ratio of characteristic condition numbers obtained for the two formulations as follows

$$R_k\left(r\right) = \frac{K_C}{K_{NC}} = \begin{cases} 2\frac{\sqrt{r^2+1}+r}{\sqrt{r^2+4}+r}, & \text{when} \quad r \leq \frac{1}{\sqrt{3}} \\ \frac{\sqrt{r^2+1}+r}{\sqrt{r^2+1}-r} \cdot \frac{2r}{\sqrt{r^2+4}+r}, & \text{when} \quad \frac{1}{\sqrt{3}} < r \leq \frac{1}{\sqrt{2}} \\ \frac{\sqrt{r^2+1}+r}{\sqrt{r^2+1}-r} \cdot \frac{\sqrt{r^2+4}-r}{\sqrt{r^2+4}+r}, & \text{when} \quad r \geq \frac{1}{\sqrt{2}} \end{cases} \tag{35}$$

R_k is also a monotonously increasing function of its argument and is always greater than 1 with an asymptote of 4 at infinity (Fig. 1b). Therefore, the non-conservative formulation results in larger local time steps and is also better conditioned for *any* values of the local flow speed and artificial compressibility parameter.

The results of the eigenvalue analysis are indicative of the differences between the two schemes. Since the solution of the Navier-Stokes equations is strongly a non-linear problem, numerical experiments are required to confirm the above analysis by comparing the convergence behaviour of the two formulations for a particular flow. Such experiments are presented in the next section.

4. NUMERICAL EXPERIMENTS

The two-dimensional flow over a backward facing step and three-dimensional flow in a channel with two inlets have been selected for investigating the accuracy and convergence behaviour of the two characteristics-based variants. The two cases are described in detail below. The convergence has been assessed using the norm of the variables derivatives in pseudo-time,

$$Conv = \max_{k,i,j} \left| \frac{f_{k,i,j}^{n+1} - f_{k,i,j}^{n}}{\Delta\tau_{i,j}} \right|, \tag{36}$$

where k stands for the primitive variable, i and j are spatial indices, and n stands for the iteration count in pseudo-time. The solution is considered to be converged when $Conv \leq 10^{-6}$. The efficiency is assessed in terms of multigrid cycles N_{mg} required to reach the above convergence threshold. Furthermore, the difference in the accuracy of the solution for the conservative and non-conservative schemes is examined using the following criterion:

$$p_{diff} = \max_{i,j} \left| \frac{p_C - p_{NC}}{p_C} \cdot 100 \right|. \tag{37}$$

The time step is defined by

$$\Delta t_{i,j} = \frac{CFL}{\left(\max_{k} |\lambda_k| \right)_{i,j}}. \tag{38}$$

where CFL is the Courant-Friedrichs-Lewy (CFL) number.

The flow over a backward-facing step has been investigated by a number of researchers both experimentally and numerically. We have performed computations for a backward facing step with inlet to channel expansion ratio 2:3 and downstream channel length equal to 60 step heights, which corresponds to the case studied experimentally by Denham and Patrick [24] and

numerically by Atkins et al. [25]. The computations have been performed on a grid containing 41×33 nodes in the inlet section and 160×49 nodes in the main channel. Simulations using coarser (81×25) and finer (321×97) grids in the main channel were also performed showing that the results between the 160×49 and 321×97 differed less than XXXX%. Therefore, it was decided all the computations to be carried out using the 160×49 grid. Computations were performed for Reynolds numbers in the range between 73 and 700. Comparisons with the experimental data of [24] are presented in Figures 2a and 2b for $Re = 73$ and $Re = 229$, respectively. The Reynolds number calculation is based on the step height and maximum velocity at the inlet profile. Note that for the case of $Re = 229$ the experimental inlet profile differs significantly from the parabolic one, therefore in order to compare with the experimental data we have used the experimental velocity profile as boundary condition at the inlet. The separated flow near the expansion at $Re = 73$ is shown in Figure 3. The value of p_{diff} did not exceed 0.09%, thus we can state that both characteristics-based schemes yield very similar results.

Figure 4 shows the convergence for two different Reynolds numbers and $CFL = 0.6$, while Figure 5 shows the number of multigrid cycles and *gain ratio*, i.e., ratio of multigrid cycles of conservative to non-conservative scheme (N_{mg}^{C}/N_{mg}^{NC}), as function of the Reynolds number. The non-conservative formulation provides faster computations (less multigrid cycles are required) and this is in accord with the eigenvalue analysis presented in the preceding section. Note that although the choice of multigrid parameters (e.g., pre- and post-relaxation iterations) effects the multigrid acceleration [12], it has been found that the relative efficiency of the non-conservative versus the conservative scheme remains the same if both schemes are employed in conjunction with the same values of multigrid parameters.

The second case considered in this study is the three-dimensional flow in a channel with with two inlets. This geometry is frequently used in microfluidic applications, such as separation and detection [26, 27, 28], micro-mixing [29, 30] and micro-fabrication [31, 32]. In many of these applications, the reagents are carried by weak solutions (see, for example [31, 32]) and the hydrodynamics of the flow, particularly the entrance length, is dominated by the solvent, which reduces the hydrodynamic problem to a single-fluid flow.

The device configuration and the development of the flow is shown in Figure 6a. The computations have been performed on a grid containing $29 \times 13 \times 13$ nodes in each inlet section and $253 \times 25 \times 13$ nodes in the main channel. Figure 6b shows the norm of deviation of the velocity profile in the main channel from the analytic steady-state solution for a rectangular channel, e.g., see [33, 34]; this is defined as $\max_{i,j} |u_{comp} - u_{an}| / u_{an} * 100$, where u_{comp} and u_{an} are the computational and analytical solutions, respectively. The difference p_{diff} of the solutions obtained by the conservative and non-conservative schemes did not exceed 0.09% thus both schemes provide similar accuracy.

Similar to the backward-facing step case, the non-conservative scheme exhibited (slightly) better convergence than the conservative scheme. The convergence histories are shown in Figure 7 for computations performed at two different Reynolds numbers. Figure 8 shows the number of multigrid cycles and *gain ratio* as function of the Reynolds number. The *gain ratio* is lower than the the backward-facing step case, but it is greater than 1 for all Reynolds numbers considered here. Finally, the number of multigrid cycles for the conservative and non-conservative schemes are reported in Tables I and II for three-dimensional computations using different CFL numbers. The results show consistently that the non-conservative formulation is slightly faster. Similar to the backward-facing step case, the convergence results for the

three-dimensional flow are in agreement with the eigenvalue analysis of Section 3.

All computations were performed on a Sun w2100z workstation with AMD Opteron 252 processor. For the backward-facing step and converging channel cases each multigrid cycle took (on average) 1.77 seconds and 17.42 seconds, respectively, according to Fortran CPU intrinsic procedure.

5. CONCLUDING REMARKS

Non-conservative and conservative formulations of characteristics-based numerical reconstructions have been derived and assessed for their accuracy and efficiency in two and three dimensional incompressible flows. We have shown through eigenvalue analysis that the two schemes should exhibit different convergence and have validated this outcome against numerical experiments.

The numerical experiments show that the conservative and non-conservative formulations provide the same accuracy but they differ in terms of convergence. The non-conservative scheme appears to be faster (or slightly faster) than the conservative version for all Reynolds numbers and flow cases considered in this study.

Finally, we note that the analysis presented in this paper can also be applicable to other high-resolution schemes and Riemann solvers that involve cell face numerical reconstruction of the primitive variables.

ACKNOWLEDGEMENT

The financial support from the Engineering and Physical Sciences Research Council (GR/S13668) is

greatly acknowledged.

REFERENCES

1. Chorin AJ. A numerical method for solving incompressible viscous ow problems. Journal of Computational Physics 1967; 2:12–26.
2. A. J. Chorin. Numerical solution of the Navier-Stokes equations. *Mathematics of Computation*, 22:745–762, 1968.
3. D. Drikakis and W. Rider, *High-Resolution Methods for Incompressible and Low-Speed Flows*, (Springer, 2004)
4. A. S. Almgren, J. B. Bell, and W. G. Szymczak. A numerical method for the incompressible Navier-Stokes equations based on an approximate projection. *SIAM Journal of Scientific Computing*, 17:358–369, 1996.
5. J. B. Bell, P. Colella, and H. M. Glaz. A second-order projection method of the incompressible Navier-Stokes equations. *Journal of Computational Physics*, 85:257–283, 1989.
6. F. H. Harlow and J. E. Welch. Numerical calculation of time-dependent viscous incompressible flow of fluid with a free surface. *Physics of Fluids*, 8:2182–2189, 1965.
7. Nithiarasu P., "An efficient artificial compressibility (AC) method based on the characteristic based split (CBS) method for incompressible flows", Int. J. Num. Meth. Engng., v. 56, pp. 1815-1845, 2003
8. Nithiarasu P., Mathur J.S., Weatherill N.P. and Morgan K., "Three-dimensional incompressible ow calculations using the characteristic based split (CBS) scheme", Int. J. Numer. Meth. Fluids, v. 44, pp. 1207-1229, 2004
9. Malan A. G., Lewis R. W. and Nithiarasu P., "An improved unsteady, unstructured, articial compressibility, nite volume scheme for viscous incompressible ows: Part I. Theory and implementation", Int. J. Numer. Meth. Engng 2002; 54:695-714
10. Malan A. G., Lewis R. W. and Nithiarasu P.,"An improved unsteady, unstructured, articial compressibility, nite volume scheme for viscous incompressible ows: Part II. Application", Int. J. Numer. Meth. Engng 2002; 54:715-729
11. D. Drikakis, O. P. Iliev, and D. P. Vassileva. Acceleration of multigird flow computations through dynamic adaptation of the smoothing procedure. *Journal of Computational Physics*, 165:566–591, 2000.

12. D. Drikakis, O. P. Iliev and D.P. Vassileva, A nonlinear multigrid method for the three-dimensional incompressible Navier-Stokes Equations, J. Comput. Phys. 146, 301 (1998)

13. D. Drikakis, P. A. Govatsos and D. E. Papatonis, A characteristic-based method for incompressible flows, Int. J. Num. Methods Fluids 19, 667 (1994)

14. A. Eberle, Characteristic flux averaging approach to the solution of Euler's equations, VKI Lecture Series, Computational Fluid Dynamics 1987-04, 1987

15. S. Pal, S. Patel, D. Drikakis, Effect of anastomosis on fluid flow through the arterial network of a rectus abdominis free flap, British Journal of Anaesthesia, 93: 167-168, 2004

16. P. Neofytou, D. Drikakis, ?Effects of blood models on flows through a stenosis?, Int. J. Numerical Methods in Fluids, 43, 597-635, 2003

17. Baili Zhang and Yong Zhao, "Simulations of flow through fluid/porous layers by a characteristic-based method on unstructured grids", Int. J. Numer. Meth. Engng, v. 50, pp. 2443-2457, 2001

18. Y. Zhao and C. H. Tai. High-order characteristics-based method for incompressible flow computation on unstructured grids. *AIAA Journal*, 39(7):1280–1287, 2001.

19. P. A. Govatsos and D. E. Papantonis. A characteristic based method for the calculation of three-dimensional, incompressible and steady flows in hydraulic turbomachines and installations. *International Journal for Numerical Methods in Fluids*, 34:1–30, 2000.

20. F. Mallinger and D. Drikakis. Instability in three dimensional unsteady stenotic flows. *International Journal of Heat and Fluid Flow*, 23:657–663, 2002.

21. E. Shapiro and D. Drikakis, "Artificial Compressibility, Characteristics-Based Schemes for Variable Density, Incompressible, Multi-Species Flows. Part I. Derivation of Different Formulations and Constant Density Limit", J. Comp. Phys., in print, doi:10.1016/j.jcp.2005.05.001, 2005

22. E. Shapiro and D. Drikakis, "E. Shapiro and D. Drikakis, "Artificial Compressibility, Characteristics-Based Schemes for Variable Density, Incompressible, Multi-Species Flows. Part II. Multigrid Implementation and Numerical Tests.", J. Comp. Phys., in print, doi:10.1016/j.jcp.2005.05.002 , 2005

23. C-W. Shu and S. Osher, Efficient implementation of essentially non-oscillatory shock capturing schemes, J. Comput. Phys. 77, 439

24. M.K. Denham and M.A. Patrick, "Laminar Flow over a downstream-facing step in a two-dimensional flow channel",Trans. Inst. Chem. Eng., v. 52(4), 361-367 (1974)

25. D.J. Atkins, S.J. Maskell and M.A. Patrick, "Numerical predition of separated flows", Int. J. Num. Methods in Engineering, v. 15, pp. 129-144, 1980

26. Weigl B.H., Yager P., "Microfluidic diffusion-based separation and detection", Science, v. 15, pp. 346-347, January 1999

27. TeGrotenhuis W.E., Cameron R.J., Viswanathan V.V., Wegeng R.S., "Solvent Extraction and Gas Absorption Using Microchannel Contactors", in Microreaction Technology: Industrial Prospects, ed. by W. Ehrfeld, Springer-Verlag Telos, pp. 541-550, 2000

28. Wong P.K., Lee Y-K., Ho C-M., Deformation of DNA molecules by hydrodynamic focusing. J. Fluid Mech. 2003; 497: 55-65.

29. Deshmukh, A., Liepmann, D. and Pisano, A. P., (2001) "Characterization of a Micro-Mixing, Pumping, and Valving System," Proceedings of the 11th International Conference on Solid State Sensors and Actuators (Transducers '01), Munich, Germany, June 10-14, 2001, 950-953.

30. Engler M., Kockmann N., Kiefer T., Woias P., "Numerical and Experimental Investigations on Liquid Mixing in Static Micro Mixers", Chemical Engineering Journal CEJ 101, 2004, pp. 315-322

31. Kenis P.J., Ismagilov R.F., Whitesides G.M., "Microfabrication inside capillaries using multiphase laminar flow patterning", *Science*, vol. 285, pp. 83-85, 1999

32. Gravesen P., Branebjerg J. and Jensen O.S. "Microfluidics - a review", J. Micromech. Microeng., v. 3, pp. 168-182, 1993

33. T.S. Lundgren, E.M. Sparrow and J.B. Starr, "Pressure drop due to the entrance region in ducts of arbitrary crossection", J. Basic Eng., v. 86, pp. 620-626, 1964

34. W. M. Rohsenow, J. P. Hartnett, E. N. Gani, "Handbook of heat transfer fundamentals", 2nd Edition, New York: McGraw-Hill, 1985

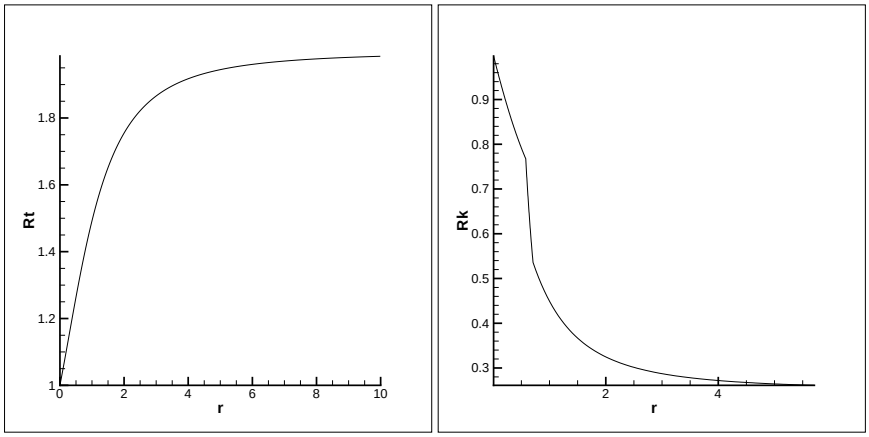

(a) Ratio of spectral radii (Eq. 34)

(b) Ratio of characteristic condition number (Eq. 35)

Figure 1. Spectral characteristics as obtained from the eigenvalue analysis for the conservative and non-conservative characteristics-based schemes.

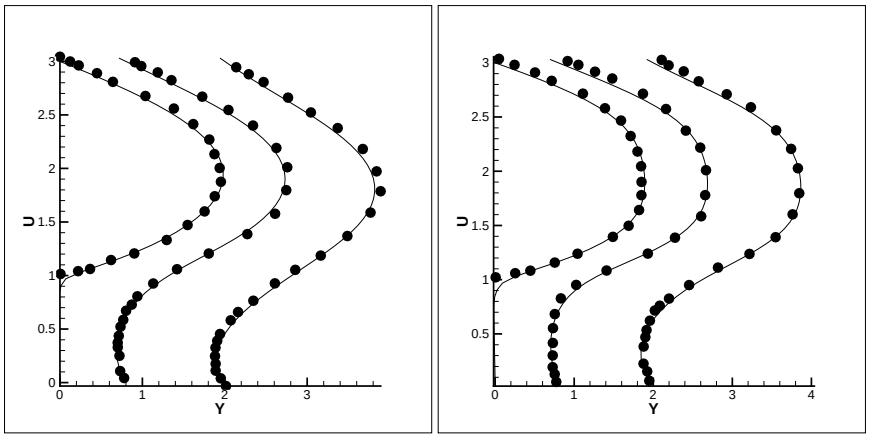

(a) Re=73 (b) Re=229

Figure 2. Comparison of numerical and experimental results [24] for the velocity profiles near the backward-facing step. The conservative and non-conservative schemes provided very similar accuracy with $p_{diff} < 0.09\%$ (see text for details).

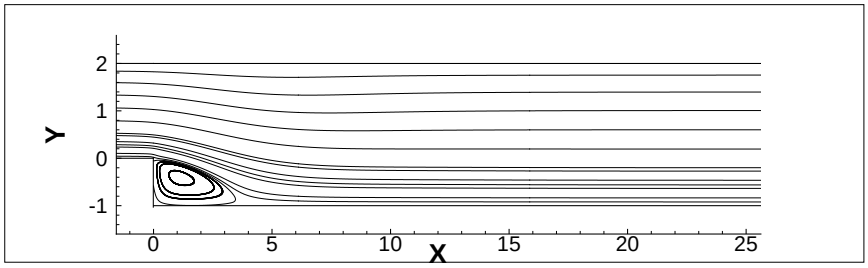

Figure 3. Separated flow near the expansion at $Re = 73$

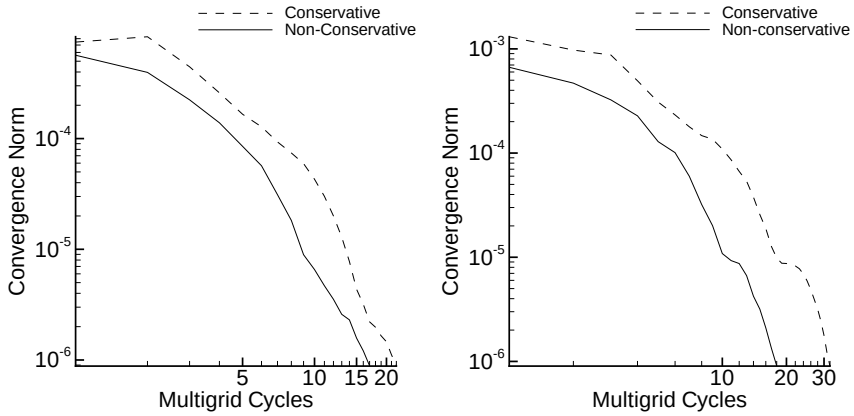

(a) Re=73 (b) Re=700

Figure 4. Convergence histories for the backward-facing step flow at two different Reynolds numbers.

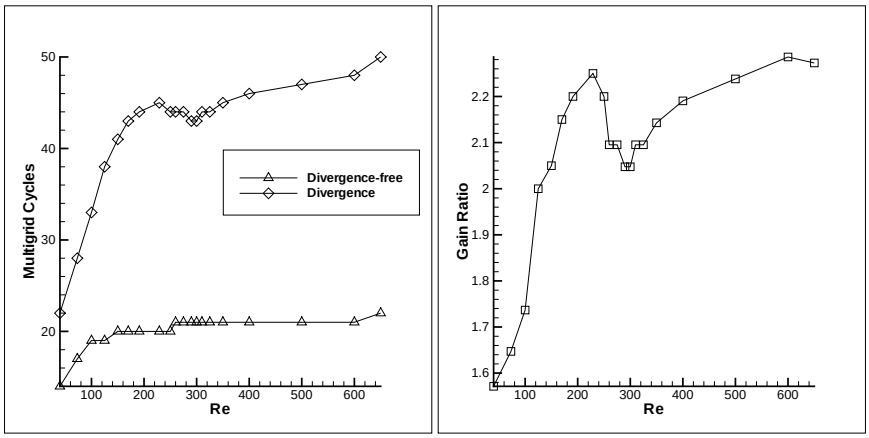

(a) Number of MG cycles required to reach convergence

(b) Gain ratio

Figure 5. Number of multigrid cycles and *gain ratio*, i.e., ratio of multigrid cycles of conservative to non-conservative scheme (N_{mg}^{C}/N_{mg}^{NC}), as function of the Reynolds number.

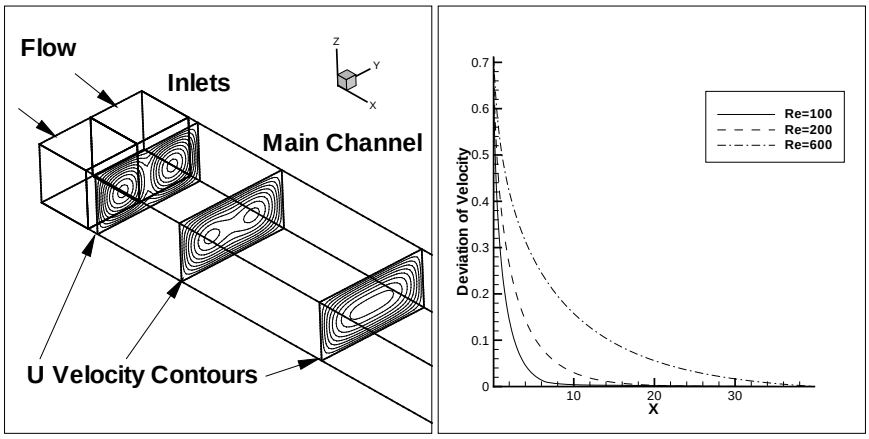

(a) Geometry and u-velocity contours (b) Velocity front development

Figure 6. Three-dimensional flow in a channel with two inlets

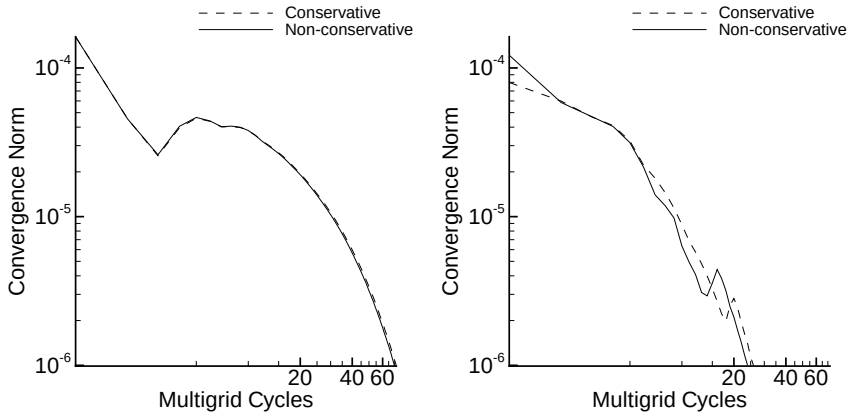

(a) Re=100 (b) Re=700

Figure 7. Convergence histories for the three-dimensional flow at two different Reynolds numbers.

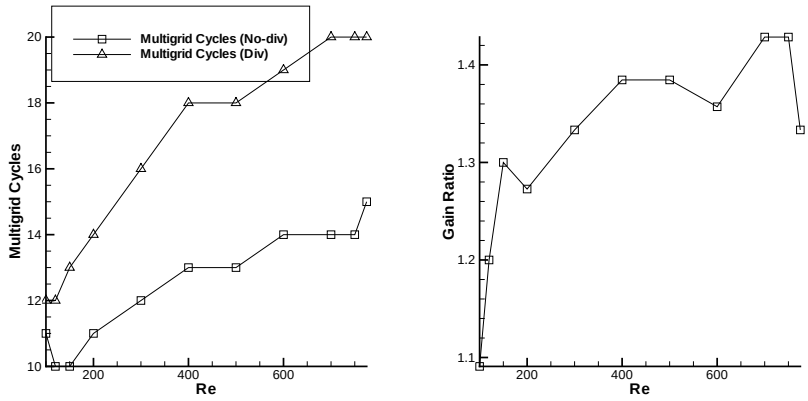

(a) Number of MG cycles required to reach convergence

(b) Gain ratio

Figure 8. Number of multigrid cycles and *gain ratio*, i.e., ratio of multigrid cycles of conservative to non-conservative scheme (N_{mg}^{C}/N_{mg}^{NC}), as function of the Reynolds number, for the three-dimensional flow case.

CFL	0.6	0.7	0.75
Conservative	72	63	59
Non-conservative	71	62	58

Table I. Number of multigrid cycles for the three-dimensional flow at $Re = 100$.

CFL	0.6	0.7	0.75
Conservative	26	24	22
Non-conservative	24	20	18

Table II. Number of multigrid cycles for the three-dimensional flow at $Re = 700$.